Multifractality in Quasienergy Space of Coherent States as a Signature of Quantum Chaos

Qian Wang [1,2,*] and **Marko Robnik** [1]

1   CAMTP-Center for Applied Mathematics and Theoretical Physics, University of Maribor,
SI-2000 Maribor, Slovenia; Robnik@uni-mb.si
2   Department of Physics, Zhejiang Normal University, Jinhua 321004, China
*   Correspondence: qwang@zjnu.edu.cn

Abstract: We present the multifractal analysis of coherent states in kicked top model by expanding them in the basis of Floquet operator eigenstates. We demonstrate the manifestation of phase space structures in the multifractal properties of coherent states. In the classical limit, the classical dynamical map can be constructed, allowing us to explore the corresponding phase space portraits and to calculate the Lyapunov exponent. By tuning the kicking strength, the system undergoes a transition from regularity to chaos. We show that the variation of multifractal dimensions of coherent states with kicking strength is able to capture the structural changes of the phase space. The onset of chaos is clearly identified by the phase-space-averaged multifractal dimensions, which are well described by random matrix theory in a strongly chaotic regime. We further investigate the probability distribution of expansion coefficients, and show that the deviation between the numerical results and the prediction of random matrix theory behaves as a reliable detector of quantum chaos.

Keywords: quantum chaos; multifractal analysis; kicked top; coherent states

1. Introduction

Quantum chaos plays a crucial role in many fields of physics, such as quantum statistics [1–5], quantum information science [6–13], and high-energy physics [14–16]. In particular, chaos of interacting quantum systems, dubbed as many-body quantum chaos, has attracted significant attention in recent years [17–23]. However, in contrast to classical chaos, which is well defined as the hypersensitivity to the initial condition [24–26], the definition of the quantum chaos in a time-dependent domain is still lacking, due to the fact that there is no quantum analog of classical trajectories in general quantum theory. In this regard, studies of OTOC (out-of-time ordered correlator) are highly relevant (see Section 3). Therefore, the questions of how the chaotic dynamics manifests itself in quantum systems and how to diagnose the quantum chaos immediately and naturally arise.

There are several ways to detect quantum chaos, which probe the effects of chaos on quantum systems from different aspects, the most popular one being the level spacing statistics [27–34]. The BGS conjecture [28] allows us to identify a given quantum system as chaotic system when its level spacing statistics is identical to the prediction of random matrix theory (RMT) [35]. Besides the level spacing statistics, the statistics of eigenvectors of quantum Hamiltonian can also be used as a benchmark to verify quantum chaos [32,36–41]. For quantum chaotic systems, their eigenfunction statistics is also well described by RMT.

A drawback of the above-mentioned quantum chaos indicators is that they only reveal the overall behaviors and cannot probe local properties of quantum chaotic systems. Since a generic system usually has a structured phase space with coexistence of regular and chaotic regions rather than a featureless fully developed chaotic region, it is highly desirable to investigate such quantities that enable us to analyze the local chaotic behaviors of a quantum system. With the help of coherent states (or localized wave packets), the local chaotic behaviors of quantum systems have been extensively explored in a variety

of works [42–49]. Here, by considering the kicked top model, we are interested in how to reveal the phase space structures and the degree of chaos by means of multifractality of coherent states.

As a general phenomenon in nature, multifractality characterizes a wide range of complex phenomena from turbulence [50] to the chemistry [51] and financial markets [52]. It has been proven that the multifractal analysis also acts as a powerful tool to understand disorder induced metal-insulator transition in both single- and many-particle Hamiltonians [53–58]. The multifractality is also presented in the ground state of quantum many-body systems and determines the physics of ground state quantum phase transition [59–62]. In addition, multifractal analysis of quantum states of random matrix models [63–67], chaotic quantum many-body systems [68,69], and open quantum systems [70] have been studied. In the present work, the fractal properties of the coherent states are examined in order to identify both the local and global signatures of quantum chaos.

We perform multifractal analysis of coherent states by expanding them on the basis of the eigenstates of the Floquet operator. To quantify the character of multifractality, we consider the so-called multifractal dimensions D_q, which characterize the structure of a quantum state in Hilbert space. For fully chaotic states, $D_q = 1$; for localized states, $D_q = 0$ with $q \geq 0$; and for the multifractal states, $0 < D_q < 1$ is a function of q [58,69]. In the kicked top model, we show that the multifractal properties of coherent states strongly depend on the chaotic behavior of its classical counterpart. We find that the multifractal dimensions exhibit a similar transition as observed in phase-space portraits and Lyapunov exponents when the system varies from regular to mixed-phase and globally chaotic dynamics. In particular, we demonstrate that the structure of classical mixed phase space can be clearly distinguished by the properties of multifractal dimensions. We also show that coherent states within the strong chaotic regime become ergodic as the system size goes to infinity, as expected from RMT predictions. On the contrary, coherent states in a regular regime still behave as multifractal states even in the thermodynamic limit. By exploring the probability distribution of the expansion coefficients, we demonstrate why the multifratal dimensions of coherent states are not zero in the regular regime and why RMT predictions on the behavior of multifractal dimensions are reliable in the fully chaotic regime.

The remainder of this article is organized as follows. In Section 2, we introduce the kicked top model, derive the stroboscopic evolution of the angular momentum for both quantum and classical cases, and analyze the classical and quantum chaotic behaviors. In Section 3, we present our numerical results in detail for the multifractal analysis of coherent states and discuss the manifestation of phase space features and onset of chaos in behavior of multifractal dimensions. Finally, we make some concluding remarks and summarize our results in Section 4.

2. Kicked-Top Model

As a paradigmatic model for both theoretical [7–11,71–78] and experimental [79–82] studies of quantum chaos, the kicked top model consists of a larger spin with total angular momentum j whose dynamics is captured by the following Hamiltonian (throughout this work, $\hbar = 1$) [10,71]:

$$H = \alpha J_x + \frac{\kappa}{2j} J_z^2 \sum_{n=-\infty}^{n=+\infty} \delta(t-n), \tag{1}$$

where $J_a (a = x, y, z)$ are the components of the angular momentum operator **J**. The first term in the Hamiltonian represents the free precession of the spin around the x axis at a rate α, while the periodic δ kicks with strength κ, the second term in Equation (1), periodically generates an impulsive rotation about the z axis by an angle $(\kappa/2j)J_z^2$, with n being the number of kicks. Here, the time period between two successive kicks has been set to

unity. The time evolution operator corresponding to above Hamiltonian is the Floquet operator [71]

$$\mathcal{F} = \exp\left(-i\frac{\kappa}{2j}J_z^2\right)\exp(-i\alpha J_x). \tag{2}$$

In the numerical calculation, the Floquet operator should be expressed in a certain representation. To this end, we employ the Dicke states $\{|j, m\rangle; (m = -j, -j+1, \ldots, j)\}$, that satisfy $\mathbf{J}^2|j, m\rangle = j(j+1)|j, m\rangle$ and $J_z|j, m\rangle = m|j, m\rangle$. Then, the matrix elements of the Floquet operator are given by

$$\langle j, m|\mathcal{F}|j, m'\rangle = \exp\left[-i\frac{\kappa}{2j}m^2\right]d_{mm'}^{(j)}(\alpha), \tag{3}$$

where

$$d_{mm'}^{(j)} = \langle j, m|e^{-i\alpha J_x}|j, m'\rangle = \sum_{k_x=-j}^{k_x=j}e^{-i\alpha k_x}\langle j, m|j, k_x\rangle\langle j, k_x|j, m'\rangle, \tag{4}$$

is the so-called Winger d-function [72], with $|j, k_x\rangle$ being the eigenstates of J_x, so that $J_x|j, k_x\rangle = k_x|j, k_x\rangle$ and $-j \le k_x \le j$. As the magnitude of spin operator is a conserved quantity, the matrix dimension is equal to $2j+1$. Moreover, as the Floquet operator in Equation (2) also conserves parity $\Pi = e^{i\pi(J_x+j)}$, its matrix space can be further split into even- and odd-parity subspaces with dimensions $\mathcal{D}_{even} = j+1$ and $\mathcal{D}_{odd} = j$, respectively.

For an arbitrary initial state $|\psi_0\rangle$, the evolved state after the nth kick is given by

$$|\psi_n\rangle = \mathcal{F}^n|\psi_0\rangle. \tag{5}$$

The expected values of the angular momentum operators are, therefore, evolved as follows

$$\langle J_a(n)\rangle = \langle\psi_n|J_a|\psi_n\rangle = \langle\psi_0|\mathcal{F}^{\dagger,n}J_a(0)\mathcal{F}^n|\psi_0\rangle, \tag{6}$$

where $J_a(n)(a = x, y, z)$ denotes the ath components of the spin operator $\mathbf{J}$ at $t = n$. Hence, the stroboscopic evolution of the spin operators can be written as

$$J_a(n+1) = \mathcal{F}^{\dagger}J_a(n)\mathcal{F}. \tag{7}$$

By using the operator identity,

$$e^{\lambda A}Be^{-\lambda A} = B + \lambda[A, B] + \frac{\lambda^2}{2}[A, [A, B]] + \ldots \tag{8}$$

the explicit form of the quantum iterated map reads [71,72,78]

$$J_x(n+1) = \frac{1}{2}\{J_x(n) + i[J_y(n)\cos\alpha - J_z(n)\sin\alpha]\}$$
$$\times \exp\left[i\frac{\kappa}{2j}\{2[J_y(n)\sin\alpha + J_z(n)\cos\alpha] + 1\}\right] + \text{H.c.} \tag{9}$$

$$J_y(n+1) = \frac{1}{2i}\{J_x(n) + i[J_y(n)\cos\alpha - J_z(n)\sin\alpha]\}$$
$$\times \exp\left[i\frac{\kappa}{2j}\{2[J_y(n)\sin\alpha + J_z(n)\cos\alpha] + 1\}\right] + \text{H.c.} \tag{10}$$

$$J_z(n+1) = J_y(n)\sin\alpha + J_z\cos\alpha. \tag{11}$$

2.1. Classical Kicked Top

The classical counterpart of the kicked top model can be obtained in the limit $j \to \infty$. To show this, we first introduce the scaled spin operators $S_a = J_a/j$, which behave as classical variables due to the vanishing commutators between them as $j \to \infty$. Then, by factorizing the mean values of the products of the angular momentum operators as

$\langle J_a J_b \rangle / j^2 = S_a S_b$ [9,78,83], it is straightforward to find that the stroboscopic map of the classical angular momentum can be written as [10]

$$
\begin{bmatrix} S_x(n+1) \\ S_y(n+1) \\ S_z(n+1) \end{bmatrix} = \mathcal{M} \begin{bmatrix} S_x(n) \\ S_y(n) \\ S_z(n) \end{bmatrix} = \begin{pmatrix} \cos \Xi_n & -\cos\alpha \sin \Xi_n & \sin\alpha \sin \Xi_n \\ \sin \Xi_n & \cos\alpha \cos \Xi_n & -\sin\alpha \cos \Xi_n \\ 0 & \sin\alpha & \cos\alpha \end{pmatrix} \begin{bmatrix} S_x(n) \\ S_y(n) \\ S_z(n) \end{bmatrix}, \quad (12)
$$

where $\Xi_n = \kappa[S_y(n)\sin\alpha + S_z(n)\cos\alpha]$. As the classical angular momentum $\mathbf{S} = (S_x, S_y, S_z)$ is a unit vector, it can be parametrized in terms of the azimuthal angle θ and polar angle ϕ as $\mathbf{S} = (\cos\phi\sin\theta, \sin\phi\sin\theta, \cos\theta)$. Hence, the classical phase space is a two dimensional space with variables $\phi = \arctan(S_y/S_x)$ and $\theta = \arccos(S_z)$.

It is known that the classical kicked top model is integrable at $\kappa = 0$ and shows increasingly chaotic behavior with increasing κ. To visualize how the value of κ affects the dynamics of the classical kicked top model, the phase-space portraits for different κ values with $\alpha = 4\pi/7$ are plotted in Figure 1a. The phase space is largely dominated by the regular orbits at small values of κ, as shown in the first two columns of Figure 1a. The phase space becomes mixed with regular regions coexisting with the chaotic sea as κ is increased; see the third column of Figure 1a. For κ increasing further, the phase space is fully covered by chaotic trajectories, and there is no visible regular island in the last column of Figure 1a.
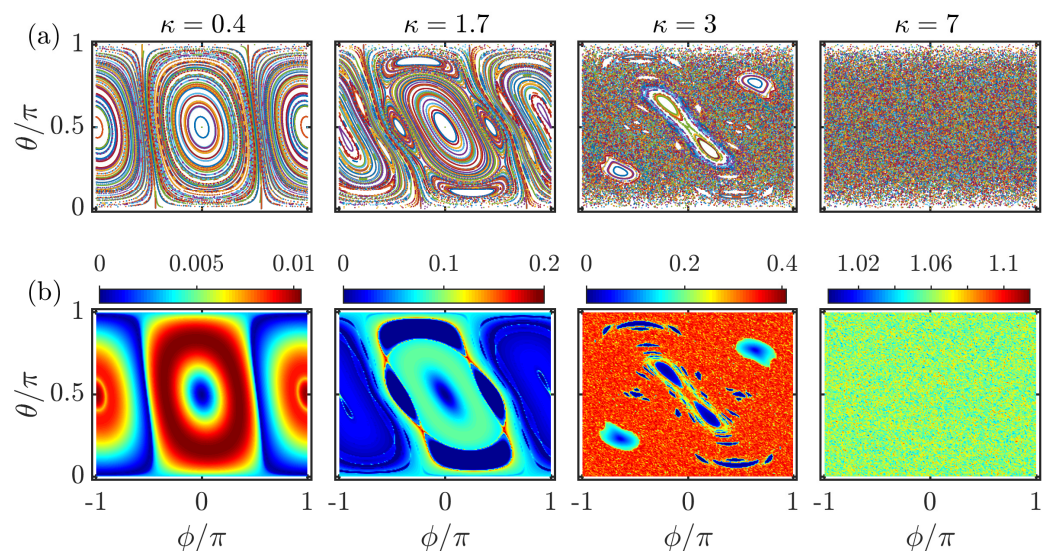
Figure 1. Row (**a**): Phase-space portraits of the classical kicked top. The classical variables (ϕ, θ) are plotted for 289 random initial conditions, each evolved for 300 kicks. Row (**b**): Color scaled plots of the largest Lyapunov exponent of the classical kicked top for different initial conditions. The largest Lyapunov exponents are calculated on a grid with 200×200 initial conditions, each evolved for 5000 kicks. The different columns correspond to (from left to right): $\kappa = 0.4, 1.7, 3$ and $\kappa = 7$. Other parameter: $\alpha = 4\pi/7$. All quantities are dimensionless.

To quantify the chaotic features observed in Figure 1a, we investigate the behavior of the largest Lyapunov exponent of the classical map in Equation (12). The largest Lyapunov exponent measures the rate of divergence between two infinitesimally close orbits of a dynamical system [78,84,85]. The largest Lyapunov exponent, therefore, estimates the level of chaos. For the classical map in Equation (12), the largest Lyapunov exponent is defined as [86]

$$
\lambda_+ = \lim_{n \to \infty} \frac{1}{n} \ln \left[\frac{||\delta \mathbf{S}(n)||}{||\delta \mathbf{S}(0)||} \right], \quad (13)
$$

where the Oseledets ergodic theorem [87] guarantees the existence of the limit. Here, the 3-dimensional vector $\delta\mathbf{S}(n)$ is the tangent vector associated with $\mathbf{S}(n)$ and satisfies the following tangent map

$$\delta\mathbf{S}(n+1) = \mathcal{T}[\mathbf{S}(n)]\delta\mathbf{S}(n) = \left[\frac{\partial\mathbf{S}(n+1)}{\partial\mathbf{S}(n)}\right]\delta\mathbf{S}(n), \tag{14}$$

with initial condition $\delta\mathbf{S}(0)$. Then, the largest Lyapunov exponent of the classical kicked top can be calculated as [78,88]

$$\lambda_+ = \ln\left[\lim_{n\to\infty}(\mu_+)^{1/n}\right], \tag{15}$$

where μ_+ denotes the largest eigenvalue of the matrix $\prod_{\ell=1}^{n}\mathcal{T}[\mathbf{S}(\ell)]$. In the limit of strong chaotic dynamics $\kappa\to\infty$, it has been found that the largest Lyapunov exponent has the following approximate expression [88]

$$\lambda_+^{\infty} = \ln(\kappa\sin\alpha) - 1, \tag{16}$$

where $\sin\alpha > 0$. It has been shown that the classical map in Equation (12) has no fully developed chaos for the cases of $\alpha = k\pi$ with $k = 0, 1, 2, \ldots$ [89]. This is due to the fact that the angle θ either keeps fixed at $\arccos[S_z(0)]$ or oscillates between $\arccos[S_z(0)]$ and $\pi - \arccos[S_z(0)]$ in these cases. On the other hand, the cases of $\alpha = (2k+1)\pi/2$ allow the strongest chaotic dynamics for classical kicked top.

In the row (b) of Figure 1, the largest Lyapunov exponents for different initial points in the $\phi - \theta$ plane corresponding to the same values of κ used in row (a) are plotted. By comparing Figure 1a,b, we found that the largest Lyapunov exponents demonstrated remarkable resemblance with the corresponding classical phase portraits. The dominated regular orbits at small κ in the phase space leads to the tiny values of the largest Lyapunov exponents, as seen in the first two columns of Figure 1b. However, the fully chaotic phase space at $\kappa = 7$ is clearly manifested by larger values of the largest Lyapunov exponent, which shows a uniform distribution in the phase space (see the last column in Figure 1b). In particular, the regular regions in the mixed phase space are identified by $\lambda_+ = 0$, as depicted in the third column of Figure 1b.

To further reveal the effect of the kicking strength on the overall degree of chaos in the classical kicked top, we consider the phase-space-averaged largest Lyapunov exponent $\bar{\lambda}_+$, which is defined as

$$\bar{\lambda}_+ = \frac{1}{4\pi}\int dS\lambda_+, \tag{17}$$

where $dS = \sin\theta d\theta d\phi$ is the area element (or Haar measure) in the phase space [90]. It is interesting to note that $\bar{\lambda}_+$ can be considered as the rescaled Kolmogorov–Sinai (KS) entropy h_{KS} [91,92], as according to the Pesin formula [93], h_{KS} of the kicked top model is equal to the sum of the largest Lyapunov exponents, so that $h_{KS} = \int dS\lambda_+$.

We plot $\bar{\lambda}_+$ as a function of κ for different values of α in Figure 2a. From this figure, we see that $\bar{\lambda}_+$ exhibits a rapid growth with increasing κ when $\kappa > \kappa_c$, regardless of the value of α. Here, κ_c is defined as a threshold at which $\bar{\lambda}_+|_{\kappa=\kappa_c} = 0.002$. This implies the onset of chaos in the classical kicked top for $\kappa > \kappa_c$. We further observe that with change of α there is a variation in the value of κ_c. Figure 2b depicts $\bar{\lambda}_+$ as a function of α and κ. We make several observations from Figure 2b. First, the behavior of $\bar{\lambda}_+$ shows a symmetry with respect to $\alpha = \pi$. This is because for the classical map in Equation (12), $\alpha \to \alpha + \pi$ is equivalent to the transformation $S_x \to -S_x$, $S_y \to -S_y$ and $S_z \to -S_z$, which keeps the largest Lyapunov exponent unchanged [90]. Second, as the classical kicked top is integrable at $\alpha = 0, \pi, 2\pi$, we have $\bar{\lambda}_+ = 0$ for these values of α, regardless of κ. Finally, for $0 < \alpha < \pi$, even though the sharp growth behavior of $\bar{\lambda}_+$ with increasing κ for $\kappa > \kappa_c$ is independent of α, there is a strong dependence of κ_c on α, as we have already seen in Figure 2a. The white dot-dashed curve in Figure 2b shows how α affects the value of κ_c. By confining to

the range $0 < \alpha < \pi$, we see that κ_c is firstly increased with increasing α and it reaches its maximal value at $\alpha = \pi/2$, and then starts to decrease as α increases further. The maximal value of κ_c at $\alpha = \pi/2$ results from the additional symmetry of the system [71], which leads to the onset of chaos occurring later than in the cases with other values of α. Without loss of general qualitative behavior, in the remainder of this work, we fixed $\alpha = 4\pi/7$.
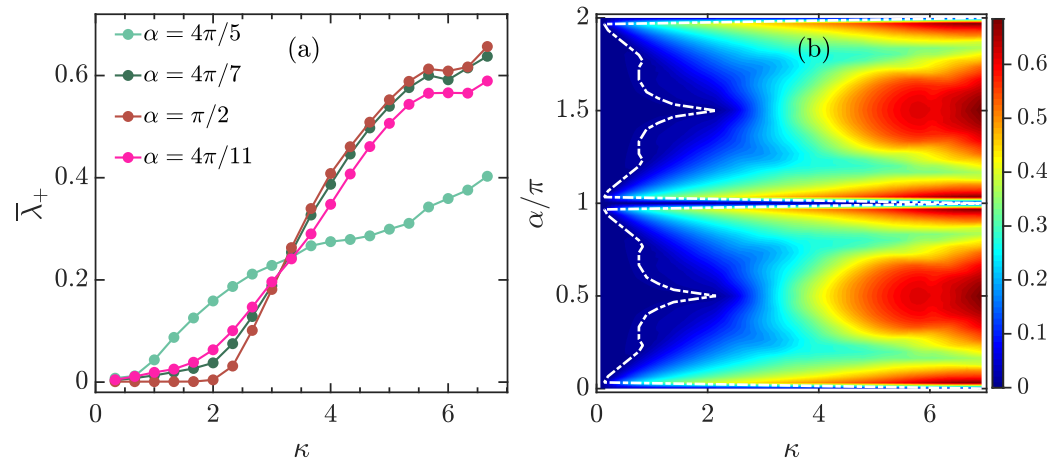
Figure 2. (**a**): Phase-space-averaged largest Lyapunov exponent $\bar{\lambda}_+$ as a function of κ for several values of α. (**b**): $\bar{\lambda}_+$ as a function of κ and α. The averaged largest Lyapunov exponents are calculated by averaging λ_+ over 40000 different initial conditions, each evolved for 5000 kicks. In (**b**), the white dot-dashed curve corresponds to the values of κ_c at which $\bar{\lambda}_+ = 0.002$. All quantities are dimensionless.

2.2. Quantum Chaos of the Kicked-Top Model

The classical chaotic features discussed above are associated with quantum chaotic behavior in quantum kicked top model. The quantum character of chaos can be detected in several ways, such as the statistical properties of eigenvalues and eigenvectors [30–32], the dynamical features of entanglement entropy [8,11,94–97], the decay in fidelity [98], the correlation hole in survival probability [99], and, in particular, the dynamics of the out-of-time-ordered correlator (OTOC) [11,96,100–103]. Among them, one of the most widely used is energy-level statistics of the quantum Hamiltonian. It is known that integrable systems allow level crossings, which give rise to Poisson distribution of the nearest level spacings [27]. On the other hand, based on the work of Wigner [104], Bohigas, Giannoni, and Schmit conjecture predicts that the energy levels in chaotic systems should exhibit level repulsion and that the distribution of the nearest level spacings follows the Wigner–Dyson distribution [28]. Here, we would like to point out that the explanation of the BGS conjecture has been first investigated through a two-point spectral correlation function [31,105], and then extended to n-point correlations with $n > 2$ [106–108] .

The spectral statistics for a periodically driven quantum system can be analyzed through the quasienergies (or eigenphases) of the Floquet operator [109]. The quasienergy spectrum of the kicked top model is obtained from the eigenphases of the Floquet operator $\mathcal{F}$ in Equation (2), and are defined as

$$\mathcal{F}|v_i\rangle = e^{iv_i}|v_i\rangle, \tag{18}$$

where v_i denotes the ith eigenphase of $\mathcal{F}$ with corresponding eigenstate $|v_i\rangle$. As $\{v_i\}$ are 2π periodic, we restrict them within the principal range $[-\pi, \pi)$.

Numerically, the spectral analysis is performed as follows. Firstly, we diagonalize $\mathcal{F}$ on the basis of $\{|j, m\rangle\}_{m=-j}^{m=j}$ and only consider the quasienergies for the Floquet eigenstates with even parity. Then, by arranging $\{v_i\}$ in ascending order, we define the gap between two consecutive levels as $d_i = v_{i+1} - v_i$. Finally, we calculate the distribution $P(s)$ of the normalized level spacings $s_i = d_i/\langle d \rangle$ [31], where $\langle d \rangle$ denotes the mean spacing. The

dependence of $P(s)$ on κ is shown in Figure 3a–d. Obviously, with increasing κ, the level spacing distribution $P(s)$ undergoes a transition from Poisson statistics $P_P(s) = e^{-s}$ to Wigner–Dyson statistics $P_{WD}(s) = (\pi/2)s \exp(-\pi s^2/4)$. This is consistent with the classical dynamics observed in Figure 1.
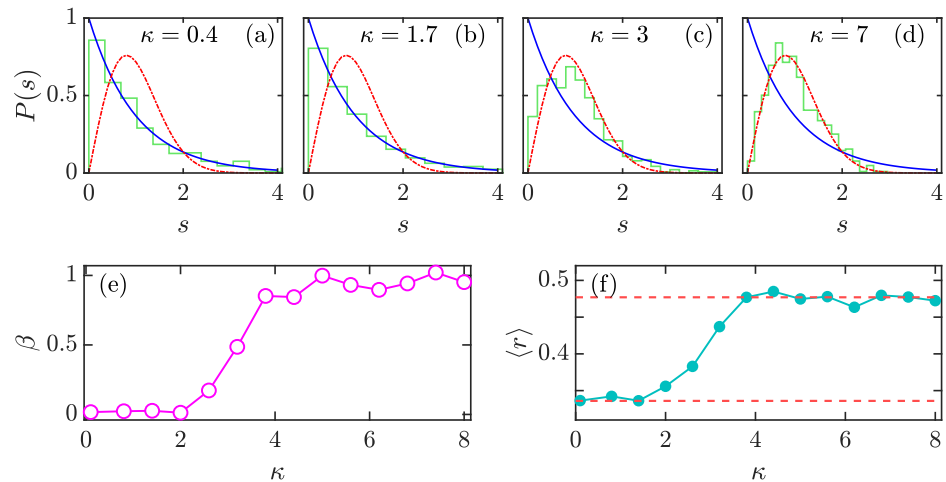
Figure 3. Level spacing distributions of the kicked top model for (**a**) $\kappa = 0.4$, (**b**) $\kappa = 1.7$, (**c**) $\kappa = 3$, and (**d**) $\kappa = 7$. The Poisson distribution is plotted as a blue solid curve, and the red dot-dashed curve denotes the Wigner–Dyson statistics. (**e**) The level repulsion exponent β as a function of κ. (**f**) Averaged level spacing ratio $\langle r \rangle$ as a function of κ. The upper (bottom) red dashed line indicates $\langle r \rangle_{COE} \approx 0.527$ ($\langle r \rangle_P \approx 0.386$). Other parameters: $j = 1000$ and $\alpha = 4\pi/7$. All quantities are dimensionless.

To estimate the degree of chaos in Floquet spectrum of the kicked top model, we fit $P(s)$ to the so-called Brody distribution defined as [30]

$$P_B(s) = b_\beta(\beta+1)s^\beta \exp[-b_\beta s^{\beta+1}], \tag{19}$$

where the factor b_β can be calculated as

$$b_\beta = \left[\Gamma\left(\frac{\beta+2}{\beta+1}\right)\right]^{\beta+1}, \tag{20}$$

where $\Gamma(x)$ is the gamma function. The parameter β, which measures the degree of repulsion between levels, is the level repulsion exponent and varies in the range $0 \leq \beta \leq 1$. For $\beta = 0$, the Brody distribution reduces to Poisson distribution, while it becomes Wigner–Dyson distribution at $\beta = 1$. Therefore, the larger β is, the stronger the chaotic spectrum is. Figure 3e plots β as a function of κ with $j = 1000$ and $\alpha = 4\pi/7$. The behavior of β nicely agrees with spectral analysis: for $\kappa \lesssim 2$, we have $\beta \approx 0$, implying the Poisson distribution of $P(s)$, while β approaches unity when $\kappa \gtrsim 5$, suggesting that the quasienergy levels have the strongest repulsion and that $P(s)$ is the Wigner–Dyson distribution. It is worth pointing out that the transition region defined as $0 < \beta < 1$ corresponds to the classical mixed-phase space with regular regions embedded in the chaotic sea. (see, e.g., the third column in Figure 1). More details about the spectral statistics in the transition region between integrability and chaos can be found in [110] and references therein. We only mention that here the Berry–Robnik level spacing distribution [111] is not yet manifested, as we are not yet in sufficiently deep semiclassical regime and observe Brody distribution instead.

Besides the level spacing distribution, the mean ratio of consecutive level spacing is another widely used detector of quantum chaos. Given the level spacing $\{d_i\}$, the mean ratio of level spacing is defined as [33,34]

$$\langle r \rangle = \frac{1}{\mathcal{N}} \sum_{i=1}^{\mathcal{N}} r_i, \quad r_i = \min\left(\frac{1}{\delta_i}, \delta_i\right),$$ (21)

where $\mathcal{N}$ is the total number of r_i and $\delta_i = d_{i+1}/d_i$. It has been demonstrated that the averaged ratio of level spacing, $\langle r \rangle$, acts as an indicator of spectral statistics. For regular systems with Poisson statistics $\langle r \rangle_P \approx 0.386$, while $\langle r \rangle_{COE} \approx 0.527$ for circular orthogonal ensemble (COE) of random matrices [34]. We plot $\langle r \rangle$ as a function of κ for $\alpha = 4\pi/7$ in Figure 3f. One can see that $\langle r \rangle$ exhibits a crossover from $\langle r \rangle_P$ to $\langle r \rangle_{COE}$ with κ increasing. This is in agreement with the behavior of $P(s)$, as observed in Figure 3a–d. Moreover, we notice that the behavior of $\langle r \rangle$ is similar to the level of the repulsion exponent β (cf. Figure 3e).

Even though the level statistics becomes a standard probe in the studies of quantum chaos, it cannot detect the local chaotic features in quantum systems. In order to characterize the phase space structure and get more insight into the quantum-classical correspondence, we consider the multifractal properties of the coherent states in the following.

2.3. Coherent States

The coherent states have wide applications in many fields [112–116]. As the uncertainty of coherent states tends to zero in the classical limit, one can expect that the phase space structure and the quantum-classical correspondence can be unveiled through appropriate properties of coherent states. For our purpose, we use the generalized SU(2) coherent spin states, which are constructed by applying an appropriate rotation on the state $|j, j\rangle$ [113,114],

$$|\vartheta, \varphi\rangle = \exp\left[i\vartheta(J_x \sin\varphi - J_y \cos\varphi)\right]|j, j\rangle,$$ (22)

where ϑ, φ provide the orientation of **J**. Further simplification of $|\vartheta, \varphi\rangle$ is available by performing Taylor expansion and the final result is given by [114,117]

$$|\vartheta, \varphi\rangle = \frac{e^{\zeta J_-}}{(1 + |\zeta|^2)^j}|j, j\rangle = \sum_{m=-j}^{j} \frac{\zeta^{j-m}}{(1 + |\zeta|^2)^j} \sqrt{\frac{(2j)!}{(j+m)!(j-m)!}}|j, m\rangle,$$ (23)

where $J_- = J_x - iJ_y$ and $\zeta = \tan(\vartheta/2)e^{i\varphi}$. It is straightforward to show that the uncertainty of the coherent spin state $|\vartheta, \varphi\rangle$ in Equation (23) vanishes as $j \to \infty$.

Here, it is worth noting that the coherent states have been exploited to explore the quantum and classical structures of the kicked-top model in several works [90,118]. The quantum-classical correspondence for various structures has been established. In particular, those works have shown that some valuable information of the scarred eigenstates, which are localized along the classical unstable periodic orbits, can be extracted from the properties of the coherent states.

3. Multifractality of Coherent States

The notion of multifractality was originally introduced to describe complex fluctuations observed in fluid turbulence [50]. It has been recognized as a valuable tool to analyze a variety of classical complex phenomena. Moreover, it has been found that the multifractal phenomenon was also visible in a quantum state. Quantum state multifractality reflects its unusual statistical properties and has attracted much attention as it plays a prominent role in the phase transitions of different quantum systems [55–61,69,119]. The characterization of the multifractality is quantified by the so-called generalized fractal dimensions, denoted

by D_q. To define D_q, let us consider a quantum state $|\Phi\rangle$ expanded in a given orthonormal basis $\{|k\rangle\}$ with dimension $\mathcal{N}$,

$$|\Phi\rangle = \sum_{k=1}^{\mathcal{N}} c_k|k\rangle, \tag{24}$$

where $c_k = \langle k|\Phi\rangle$ and satisfies $\sum_k |c_k|^2 = 1$. Then, D_q is defined as [53,69]

$$D_q = \frac{S_q}{\ln \mathcal{N}} \quad \text{and} \quad S_q = \frac{1}{1-q} \ln \left(\sum_{k=1}^{\mathcal{N}} |c_k|^{2q} \right), \tag{25}$$

where S_q is the Rényi entropy (or participation entropy). For finite $\mathcal{N}$, the values of D_q are defined in the interval $D_q \in [0,1]$ and decrease with increasing q for $q \geq 0$ [68]. The fractal dimensions, $\mathcal{D}_q^\infty$, are obtained as $\mathcal{N} \to \infty$, so that $\mathcal{D}_q^\infty = \lim_{\mathcal{N}\to\infty} D_q$ [53,68]. The degree of ergodicity of a quantum state in Hilbert space is measured by the fractal dimensions. For a perfectly localized state $\mathcal{D}_q^\infty = 0$ for $q > 0$, whereas $\mathcal{D}_q^\infty = 1 (\forall q)$ corresponds to an ergodic state. The multifractal states are the extended non-ergodic states and identified by $0 < \mathcal{D}_q^\infty < 1$.

　　Among all D_q, we focus on the cases where $q = 1, 2$, and ∞. As the Rényi entropy reduces to the Shannon entropy, $S_1 = -\sum_k |c_k|^2 \ln |c_k|^2$, in the limit $q \to 1$, the dimension D_1, also known as information dimension, controls the scaling of Shannon information entropy. For $q = 2$, $S_2 = \ln(\sum_k |c_k|^4)^{-1}$ is the logarithm of the well-known participation ratio [57,58,120], which measures the degree of delocalization of the state in Hilbert space. Hence, the exponent D_2 quantifies the scaling of the participation ratio. At $q = \infty$, the Réyni entropy turns into $S_\infty = -\ln p_m$ with $p_m = \max_k |c_k|^2$ and $D_\infty = -\ln p_m / \ln \mathcal{N}$, determining the extreme value statistics of the intensities of the quantum state.

　　In our study, we analyze the multifractal properties of the generalized SU(2) coherent spin states (cf. Equation (23)) in the eigenvectors of the Floquet operator. Therefore, we first expand $|\vartheta, \varphi\rangle$ on the basis of $\{|v_i\rangle\}$ as follows

$$|\vartheta, \varphi\rangle = \sum_i w_i |v_i\rangle, \tag{26}$$

where $w_i = \langle v_i|\vartheta, \varphi\rangle$ is the overlap between the basis vector $|v_i\rangle$ and the coherent state $|\vartheta, \varphi\rangle$, fulfilling the normalization condition $\sum_i |w_i|^2 = 1$. Then, using Equation (25), the fractal dimensions are calculated for coherent states that are centered at different points (θ, ϕ) of the classical phase space.

　　In Figure 4, we plot D_1, D_2, and D_∞ as a function of ϕ and θ for different kicking strengths κ. By comparing with the classical phase space portraits in Figure 1a, we observe that the underlying classical dynamics has strong effects on the properties of the fractal dimensions. The regular regions around the fixed points give rise to $D_q \approx 0$, indicating the coherent states located at these points are the localized states, as seen in the first and second columns of Figure 4. In the chaotic phase space, the fractal dimensions have larger values and exhibit an approximately uniform distribution in the phase space (see the last column of Figure 4). These features imply that the coherent states have high degree of ergodicity for large kicking strength. For the mixed phase space, it is evident from the third column of Figure 4 that the regular regions are identified by smaller fractal dimensions, while larger D_q correspond to the chaotic sea. The obvious correspondence between the fractal dimension and the classical phase space dynamics and the Lyapunov exponents, as shown in Figure 1a,b, suggests that D_q are particularly useful to detect the signatures of quantum chaos. We further notice that $0 < D_q < 1$ still holds even if the system is governed by regular dynamics.
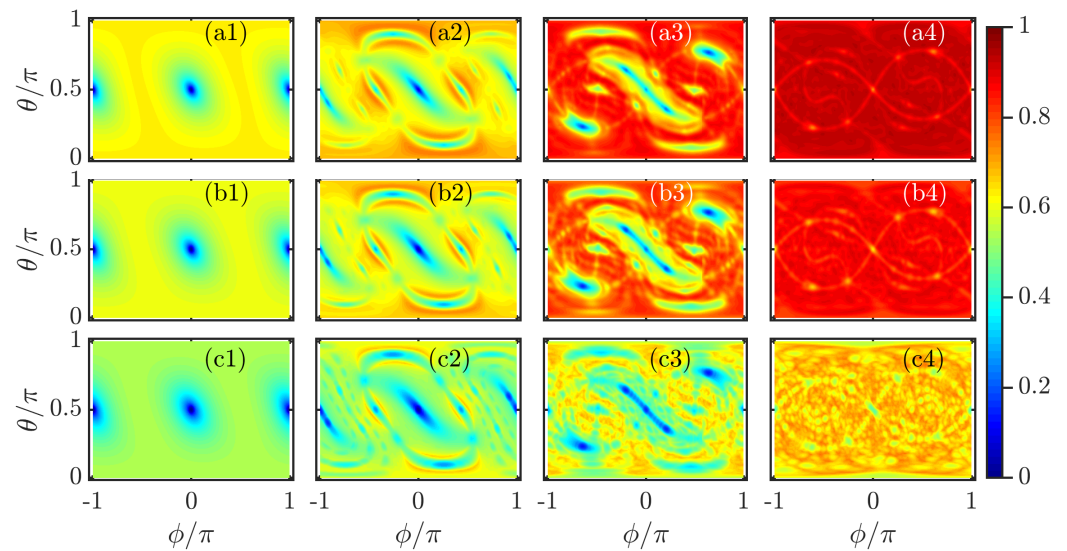
Figure 4. Color scaled plot of multifractal dimensions D_q for (**a1**–**a4**) $q = 1$, (**b1**–**b4**) $q = 2$, and (**c1**–**c4**) $q = \infty$, calculated on a grid of 100×100 coherent states. The different columns correspond to (from left to right): $\kappa = 0.4$, $\kappa = 1.7$, $\kappa = 3$, and $\kappa = 7$. Other parameters: $j = 150$ and $\alpha = 4\pi/7$. All quantities are dimensionless.

To further demonstrate that D_q can enable us to discern the regular and chaotic characters of the quantum system, we assess the phase-space-averaged fractal dimensions, defined as

$$\overline{D}_q = \frac{1}{4\pi} \int dS D_q. \tag{27}$$

Figure 5a–c show, respectively, $\overline{D}_1$, $\overline{D}_2$ and $\overline{D}_1$ as a function of κ for different system sizes j. We see that the dependence of fractal dimensions on κ is similar for different j. The fractal dimensions change slowly with increasing κ for smaller κ and exhibit a rapid growth as soon as $\kappa > 2$. Then, $\overline{D}_q$ eventually approach their saturation values when $\kappa > 5$. Moreover, we also observe that $\overline{D}_q$ are almost independent of j for $\kappa < 2$, while they increase with increasing j as long as $\kappa > 5$.
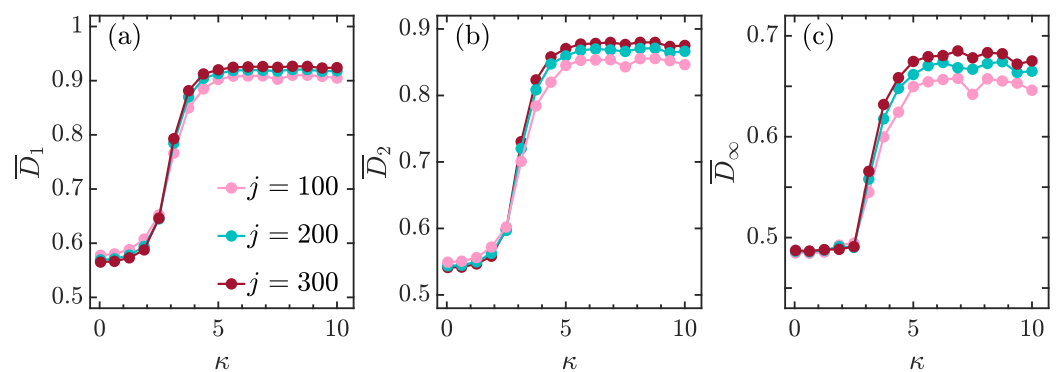
Figure 5. The variation in phase-space-averaged multifractal dimensions $\overline{D}_1$ (**a**), $\overline{D}_2$ (**b**), and $\overline{D}_\infty$ (**c**) with kicking strength κ for different j are denoted by color scales. The phase space average is performed over 10^4 coherent states in phase space. Other parameters: $\alpha = 4\pi/7$. All quantities are dimensionless.

In Figure 6, we plot the scaling of $\overline{D}_q$ with $1/\ln \mathcal{N}$ for $\kappa = 0.4$ and $\kappa = 7$. Here, $\mathcal{N}$ is the Hilbert space dimension of the system. For the regular regime with $\kappa = 0.4$ (Figure 6a), $\overline{D}_q$ follow the linear scaling of the form $\overline{D}_q = 1/2 - f_q/\ln \mathcal{N}$ with f_q depending on the value of q. In particular, the scaling behaviors of $\overline{D}_q$ imply that $\overline{D}_q$ tend to $1/2$ rather than

zero as $\mathcal{N} \to \infty$. On the other hand, according to RMT, $\overline{D}_q$ in a fully chaotic regime obey the following asymptotic behavior [68,69,121]

$$\overline{D}_q^s = \begin{cases} 1 - \dfrac{g_q}{\ln \mathcal{N}} & \text{for } q = 1, 2, \\ 1 - g_\infty \dfrac{\ln(\ln \mathcal{N})}{\ln \mathcal{N}} & \text{for } q = \infty. \end{cases} \tag{28}$$

As the kicked top becomes a strongly chaotic system at larger κ, one can expect that the scaling behaviors of $\overline{D}_q$ should be in agreement with the above results and should approach unity in the thermodynamic limit. This is indeed what we see in panel (b) of Figure 6, which shows how $\overline{D}_q$ vary with $1/\ln \mathcal{N}$ at $\kappa = 7$. A good agreement between the numerical data and $\overline{D}_q^s$ in Equation (28) leads us to conclude that the coherent states in strongly chaotic regimes become ergodic in the eigenstates of the Floquet operator.
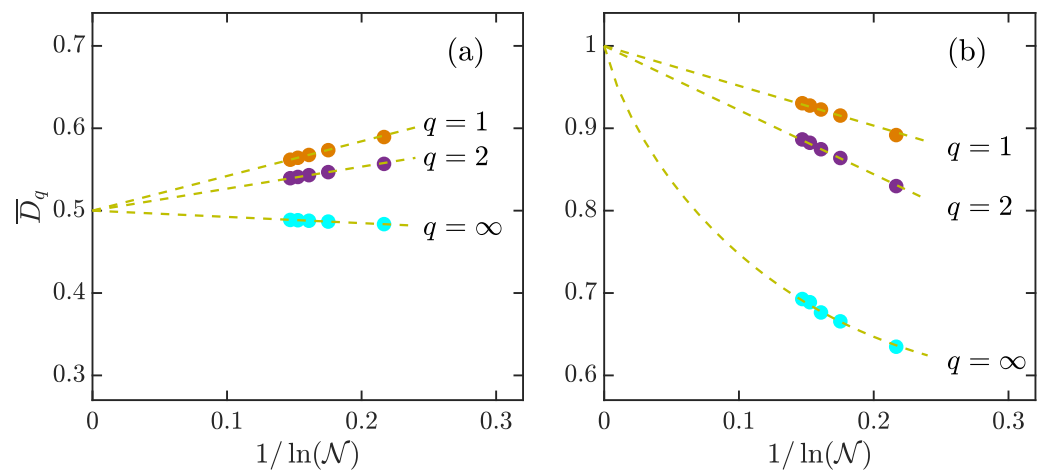
Figure 6. Phase-space-averaged fractal dimensions $\overline{D}_q$ with $q = 1, 2, \infty$ versus $1/\ln \mathcal{N}$ for $\kappa = 0.4$ (**a**) and $\kappa = 7$ (**b**). Here, $\mathcal{N}$ denotes the dimension of Hilbert space. $\overline{D}_q$ were calculated from 10^4 coherent states in phase space. Dashed lines in panel (**a**) are of the form $1/2 - f_q/\ln \mathcal{N}$, with $f_1 = 0.421$, $f_2 = 0.267$ and $f_\infty = -0.0758$. In panel (**b**), dashed lines for $q = 1, 2$ are of the form $1 - g_q/\ln \mathcal{N}$ with $g_1 = 0.484$ and $g_2 = 0.779$, while the dashed line for $q = \infty$ is given by $1 - g_\infty \ln(\ln \mathcal{N})/\ln \mathcal{N}$ with $g_\infty = 1.097$. Other parameters: $\alpha = 4\pi/7$. All quantities are dimensionless.

More insights into the ergodic property of the coherent states in the eigenvectors of the Floquet operator can be obtained through the statistics of the rescaled expansion coefficients $\{x_i = \mathcal{N}|w_i|^2\}$. For fully chaotic systems, it has been demonstrated that the probability distribution of $\{x_i\}$ for different ensembles are unified in the χ_ν^2 distribution, as shown in [35,39–42],

$$P_\nu(x) = \left(\frac{\nu}{2\langle x \rangle}\right)^{\nu/2} \frac{x^{\nu/2-1}}{\Gamma(\nu/2)} \exp\left(-\frac{\nu x}{2\langle x \rangle}\right), \tag{29}$$

where $\langle x \rangle$ is the mean value of $\{x_i\}$ and $\nu = 1, 2, 4$ for orthogonal, unitary, and symplectic ensembles, respectively. In particular, $P_\nu(x)$ turns into the well-known Porter–Thomas distribution [37] when $\nu = 1$. The width of the distribution becomes narrower with increasing ν, indicating the larger of the value of ν, the smaller the fluctuations of $\{x_i\}$.

For the coherent state considered here, the expansion coefficients are complex numbers, and their distribution in the fully chaotic regime should be expected to be given by χ_ν^2 distribution with $\nu = 2$ [38,122]. Moreover, due to the large amount of small coefficients,

we explore the distribution of $\{\ln x_i\}$ instead of $\{x_i\}$. From Equation (29), $P_\nu(\ln x)$, is given by

$$P_\nu(\ln x) = \frac{P_\nu(x)}{d \ln x / dx} = \left(\frac{\nu}{2\langle x \rangle}\right)^{\nu/2} \frac{x^{\nu/2}}{\Gamma(\nu/2)} \exp\left(-\frac{\nu x}{2\langle x \rangle}\right). \tag{30}$$

The relation $P_\nu(\ln x) = x P_\nu(x)$ implies that $P(\ln x)$ has the maximal value at $x = \langle x \rangle$.

In the main panels of Figure 7, we show $P(\ln x)$ and compare with $P_2(\ln x)$ for several values of κ. The numerical data are obtained from 10^4 coherent states that are uniformly located in the phase space. As expected, for the regular case with smaller κ values, the larger number of small coefficients leads to larger fluctuations around its averaged value and a greater deviation from $P_2(\ln x)$, as shown in Figure 7a,b. However, the peak of $P(\ln x)$ around $\ln x \sim 2$ results in moments of $P(x)$ that are q-dependent, which means non-zero multifractal dimensions $D_q(q > 0)$ at smaller κ values. With further increasing κ, the distribution of $P(\ln x)$ shifts its location to larger values of $\ln x$ and becomes narrower (Figure 7c). For even larger κ values, the distribution $P(\ln x)$ eventually converges to $P_2(\ln x)$, as visible in Figure 7d. Here, we would like to point out that the peaks observed in panels (a) and (b) of Figure 7 have nothing to do with the regularity and/or chaos. In fact, their appearance depends on the computation basis that we used to expand the quantum state, as has been stressed in [41]. The regularity of a system is only manifested in the long flat tail of $P(\ln x)$.
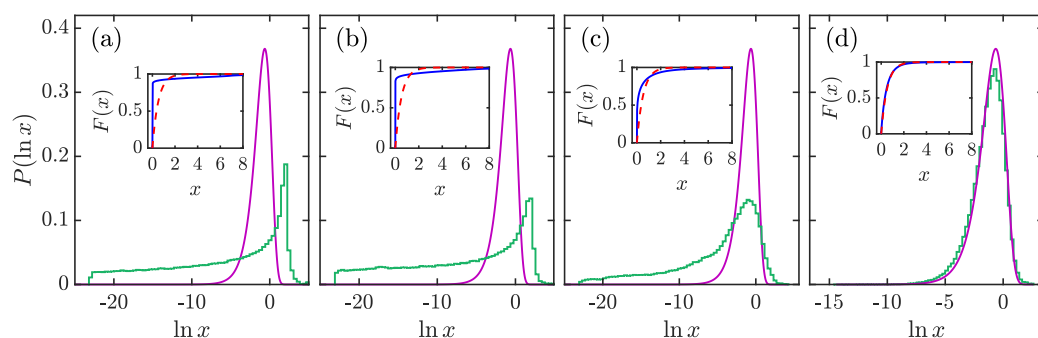
Figure 7. Histograms of $P(\ln x)$ for $\kappa = 0.4$ (**a**), $\kappa = 1.7$ (**b**), $\kappa = 3$ (**c**), and $\kappa = 7$ (**d**). The purple solid lines in the main panels denote $P_2(\ln x)$ [cf. Equation (30)]. The inset in each panel plots their cumulative distributions with blue solid curve corresponds to numerical result, while the red dashed curve represents $F_2(x)$ (cf. Equation (32)). $P(\ln x)$ has been computed from 10^4 coherent states in phase space. Other parameters: $j = 150$ and $\alpha = 4\pi/7$. All quantities are dimensionless.

The convergence between the distributions of $P(x)$ and $P_2(x)$ as κ increases is also confirmed in the behavior of the corresponding cumulative distributions. For the distribution $P(x)$, the cumulative distribution is defined as

$$F(x) = \int_0^x P(t)dt, \tag{31}$$

while the cumulative distribution of $P_\nu(x)$ is given by

$$F_\nu(x) = \int_0^x P_\nu(t)dt = \frac{\gamma[\nu/2, \nu x/(2\langle x \rangle)]}{\Gamma(\nu/2)}, \tag{32}$$

where $\gamma(s, x) = \int_0^x t^{s-1}e^{-t}dt$ is the lower incomplete gamma function. The insets in Figure 7 show $F(x)$ and $F_2(x)$ for different κ values. It can be seen that the deviation between $F(x)$ and $F_2(x)$ decreases with increasing κ, in accordance with the behavior of $P(\ln x)$ observed in the main panels.

To quantify the distance between $P(x)$ and $P_2(x)$, we use two different deviation measures, namely the square root of the Kullback–Leibler divergence (SKLD) [123,124] and the root-mean-square error (RMSE) [125,126]. For the observed distribution $P(x)$

and predicted distribution $P_\nu(x)$, the SKLD (RMSE), denoted as $\mathcal{D}_{KL}^{(\nu)}(\mathcal{R}_d^{(\nu)})$, measures the difference between observed and predicted probability (cumulative) distributions. The definitions of SKLD and RMSE are, respectively, given by

$$\mathcal{D}_{KL}^{(\nu)} = \left\{ \int_{x_0}^{x_m} P(x) \ln\left[\frac{P(x)}{P_\nu(x)}\right] dx \right\}^{1/2}, \tag{33}$$

$$\mathcal{R}_d^{(\nu)} = \left\{ \frac{1}{x_m - x_0} \int_{x_0}^{x_m} [F(x) - F_\nu(x)] dx \right\}^{1/2}, \tag{34}$$

where x_0 and x_m are the minimum and maximum values of $\{x_i\}$, respectively. Both $\mathcal{D}_{KL}^{(\nu)}$ and $\mathcal{R}_d^{(\nu)}$ are defined in the interval $\mathcal{D}_{KL}^{(\nu)}, \mathcal{R}_d^{(\nu)} \in [0, \infty)$. When $\mathcal{D}_{KL}^{(\nu)} = \mathcal{R}_d^{(\nu)} = 0$, we have $P(x) = P_\nu(x)$, whereas larger $\mathcal{D}_{KL}^{(\nu)}, \mathcal{R}_d^{(\nu)}$ values imply a larger deviation between $P(x)$ and $P_\nu(x)$.

The variation in distance between $P(x)$ and $P_2(x)$, measured by $\mathcal{D}_{KL}^{(2)}$ and $\mathcal{R}_d^{(2)}$, with κ for different j values, is shown in Figure 8. We see that $\mathcal{D}_{KL}^{(2)}$ and $\mathcal{R}_d^{(2)}$ behave in a similar way with increasing κ. For the regular regime with weak kicking strength $\kappa < 2$, both of them have high values and decrease slowly as κ increases. This means that the coherent states are far from ergodicity in the regular regime. Then, they exhibit a rapid decrease in the region $2 \lesssim \kappa \lesssim 5$, which corresponds to the crossover from the integrability to full chaos. Finally, for $\kappa > 5$, as the system becomes globally chaotic, both $\mathcal{D}_{KL}^{(2)}$ and $\mathcal{R}_d^{(2)}$ decrease to very small values and are almost independent of κ. Hence, the coherent states are ergodic states in a fully chaotic regime. Moreover, the degree of ergodicity of coherent states in a strongly chaotic regime can be enhanced by increasing the system size, as illustrated in the insets of Figure 8.
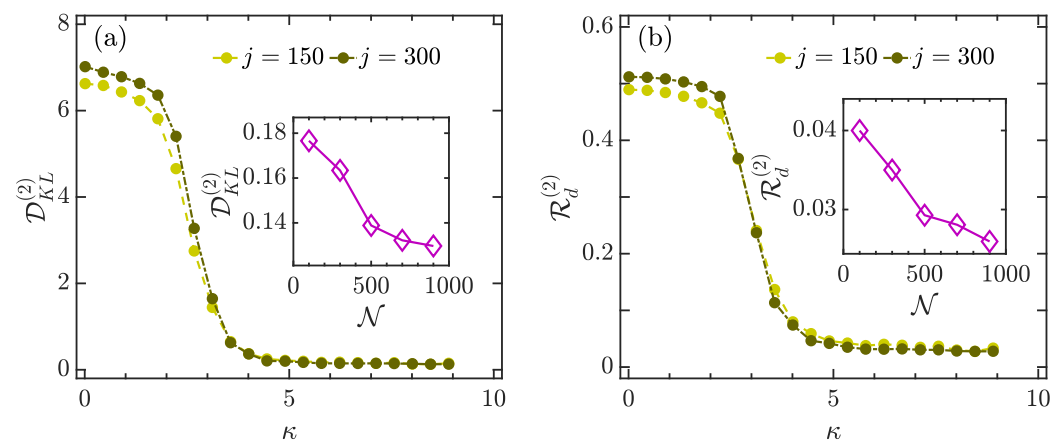
Figure 8. Panel (**a**): $\mathcal{D}_{KL}^{(2)}$ as a function of κ for different system sizes. Inset: $\mathcal{D}_{KL}^{(2)}$ as a function of Hilbert space dimension $\mathcal{N}$ with $\kappa = 8$. Panel (**b**): $\mathcal{R}_d^{(2)}$ as a function of κ for different j values. Inset: $\mathcal{R}_d^{(2)}$ versus Hilbert space dimension $\mathcal{N}$ for $\kappa = 8$. Other parameter: $\alpha = 4\pi/7$. All quantities are dimensionless.

Here, an interesting point deserves discussing, namely the connection between the fractal dimensions D_q and other quantum chaos probes. Among all detectors of quantum chaos, we focus on spectral form factor (SFF) and out-of-time-ordered correlators (OTOCs). Both of them have been extensively used in numerous recent studies [18–22,100–103,127–134].

Let us first consider the relation between D_q and SFF. The SFF is a powerful tool for detecting the spectral properties of a system and is defined as the Fourier transform of the two-point correlation function of the level density [135]. It is known that the behavior of SFF for integrable systems is drastically different from the chaotic systems, mainly due to the fact that the regular and chaotic systems have different spectral statistics [20]. This

means that the SFF can be used as an efficient and sensitive indicator of quantum chaos. As SFF measures the correlation between energy levels, while D_q characterizes the complexity of quantum states in a given basis, there is no obvious relation between them. Although, for some particular cases, D_q and SFF have been connected in several works [64,136], a more general connection between them is still an open question, beyond the scope of the present work. We will explore this subject in our future work.

We now discuss the comparison of D_q with OTOCs. As the main criterion employed to decide whether a quantum system is chaotic or not, OTOC quantifies the sensitivity with respect to the initial condition and information scrambling in quantum systems. It has been demostrated that both the early and late behaviors of OTOC serve as useful diagnostics of quantum chaos [100–103,137,138]. Since the chaotic dynamics leads to rapid growth and large long-time saturation value in the behavior of OTOC, one can, therefore, expect that the growth rate of the OTOC as well as its long-time saturation value may be correlated with D_q. However, a more detailed and general connection between them remains an open question. To date, only a formal relationship between D_2 and OTOCs has been established [139,140].

We finally point out that the degree of extension of a quantum state usually increases with the degree of chaoticity of the system. Hence, we believe that qualitatively similar results should be obtained for generic quantum states and for other quantum systems. Moreover, our main conclusions still hold if the coherent states are expanded to another more localized basis, even if the fractal dimensions are dependent on the choice of the basis.

4. Conclusions

In this work, we explored the quantum characters of chaos in the quantum kicked top model by means of multifractal analysis. The kicked top model is a prototype model in the studies of quantum chaos, and its experimental realization has been achieved in several experiments [79–82]. The signatures of classical chaos have been revealed in various works. It was known that the phase space of classical kicked top has complex structures during the transition from regular to chaotic dynamics. Therefore, understanding how to capture the local chaotic features in quantum system becomes a crucial point in order to understand the quantum-classical correspondence. Although the indicators of quantum chaos, such as level spacing statistics and mean ratio of level spacings, are able to unveil the global signatures of chaos in quantum systems, they cannot detect the local chaotic behaviors. In the present work, with the help of the generalized coherent spin states, we investigated the local chaotic properties of quantum kicked top through the multifractal dimensions of coherent states.

The multifractal analysis of the coherent states is performed by expanding them in orthonormal basis composed by the eigenstates of the Floquet operator. We explicitly demonstrated that the regular regions in the mixed phase space clearly correspond to small values of multifractal dimensions. For the strong chaotic case, the multifractal dimensions exhibit uniform distribution in phase space. Moreover, we have shown that the phase-space-averaged multifractal dimensions serve as indicators of quantum chaos. With kicking strength increasing, the averaged multifractal dimensions undergo a rapid growth, indicating the transition from regular to chaotic dynamics of the system. Coherent states within the strongly chaotic regime become ergodic, with multifractal dimensions tending to unity in the thermodynamic limit, in accordance with the predictions of RMT. However, coherent states' multifractal dimensions in the regular regime are not equal to zero. Instead, they approach a finite value as the system size goes to infinity.

To get more insight into the multifractal characters of the coherent states and their connections with the underlying chaotic dynamics, we further investigated the probability distribution of the expansion coefficients. Such distribution is expected to follow the so-called χ_ν^2 distribution for the fully chaotic systems. We have shown that the deviation between the distribution of coefficients and χ_2^2 distribution decreases as the kicking

strength is increased. For the kicking strengths that lead to the fully chaotic dynamics, the distribution of coefficients exhibits a quite good agreement with χ_2^2 distribution, implying the strong ergodicity of coherent states. On the contrary, the distribution of coefficients in the regular regime displays a remarkable difference from χ_2^2 distribution and its long flat tail reveals the localization character of coherent states. In particular, the non-zero fractal dimensions for the regular case can be understood as a consequence of the sharp peak appearing in the probability distribution of coefficients. As the existence of the peak in the distribution of coefficients for the regular regime is a basis-dependent phenomenon, one can therefore expect that the fractal dimensions in regular systems should be equal to zero if a suitable computation basis has been selected. Understanding how to identify an appropriate basis used in the multifractality analysis is an interesting topic for future studies. We also discuss how to measure the distance between the observed distribution of coefficients and the expected χ_2^2 distribution. We have shown that the transition from regular to chaotic dynamics of the system can be identified by the dramatic decrease in the behavior of different distance measures.

As a final remark, we would like to point out that the recent experimental advances enable a direct observation of multifractality of wave packets in several quantum systems [141–144]. Hence, the multifractal properties of our studied Floquet system are readily accessible for state-of-the-art experimental platforms.

Author Contributions: Q.W. performed analytical and numerical calculations. All authors have contributed to reviewing the results and final discussion. The original writing of this paper was by Q.W., with structural modifications recommended by M.R. Final checking, revision and editing by Q.W. and M.R. All authors have read and agreed to the published version of the manuscript.

Institutional Review Board Statement: Not applicable.

Informed Consent Statement: Not applicable.

Data Availability Statement: Not applicable.

Conflicts of Interest: The authors declare no conflict of interest.

References

1. Altland, A.; Haake, F. Quantum Chaos and Effective Thermalization. *Phys. Rev. Lett.* **2012**, *108*, 073601. [CrossRef]
2. Nandkishore, R.; Huse, D.A. Many-Body Localization and Thermalization in Quantum Statistical Mechanics. *Annu. Rev. Condens. Matter Phys.* **2015**, *6*, 15–38. [CrossRef]
3. D'Alessio, L.; Kafri, Y.; Polkovnikov, A.; Rigol, M. From quantum chaos and eigenstate thermalization to statistical mechanics and thermodynamics. *Adv. Phys.* **2016**, *65*, 239–362. [CrossRef]
4. Borgonovi, F.; Izrailev, F.; Santos, L.; Zelevinsky, V. Quantum chaos and thermalization in isolated systems of interacting particles. *Phys. Rep.* **2016**, *626*, 1–58. [CrossRef]
5. Deutsch, J.M. Eigenstate thermalization hypothesis. *Rep. Prog. Phys.* **2018**, *81*, 082001. [CrossRef]
6. Vidmar, L.; Rigol, M. Entanglement Entropy of Eigenstates of Quantum Chaotic Hamiltonians. *Phys. Rev. Lett.* **2017**, *119*, 220603. [CrossRef]
7. Alicki, R.; Makowiec, D.; Miklaszewski, W. Quantum Chaos in Terms of Entropy for a Periodically Kicked Top. *Phys. Rev. Lett.* **1996**, *77*, 838–841. [CrossRef] [PubMed]
8. Wang, X.; Ghose, S.; Sanders, B.C.; Hu, B. Entanglement as a signature of quantum chaos. *Phys. Rev. E* **2004**, *70*, 016217. [CrossRef] [PubMed]
9. Ghose, S.; Stock, R.; Jessen, P.; Lal, R.; Silberfarb, A. Chaos, entanglement, and decoherence in the quantum kicked top. *Phys. Rev. A* **2008**, *78*, 042318. [CrossRef]
10. Piga, A.; Lewenstein, M.; Quach, J.Q. Quantum chaos and entanglement in ergodic and nonergodic systems. *Phys. Rev. E* **2019**, *99*, 032213. [CrossRef] [PubMed]
11. Lerose, A.; Pappalardi, S. Bridging entanglement dynamics and chaos in semiclassical systems. *Phys. Rev. A* **2020**, *102*, 032404. [CrossRef]

12. Lantagne-Hurtubise, E.; Plugge, S.; Can, O.; Franz, M. Diagnosing quantum chaos in many-body systems using entanglement as a resource. *Phys. Rev. Res.* **2020**, *2*, 013254. [CrossRef]
13. Anand, N.; Styliaris, G.; Kumari, M.; Zanardi, P. Quantum coherence as a signature of chaos. *Phys. Rev. Res.* **2021**, *3*, 023214. [CrossRef]
14. Maldacena, J.; Shenker, S.H.; Stanford, D. A bound on chaos. *J. High Energy Phys.* **2016**, *2016*, 106. [CrossRef]
15. Magán, J.M. Black holes, complexity and quantum chaos. *J. High Energy Phys.* **2018**, *2018*, 43. [CrossRef]
16. Jahnke, V. Recent Developments in the Holographic Description of Quantum Chaos. *Adv. High Energy Phys.* **2019**, *2019*, 9632708. [CrossRef]
17. Stanford, D. Many-body chaos at weak coupling. *J. High Energy Phys.* **2016**, *2016*, 9. [CrossRef]
18. Chan, A.; De Luca, A.; Chalker, J.T. Solution of a Minimal Model for Many-Body Quantum Chaos. *Phys. Rev. X* **2018**, *8*, 041019. [CrossRef]
19. Kos, P.; Ljubotina, M.; Prosen, T. Many-Body Quantum Chaos: Analytic Connection to Random Matrix Theory. *Phys. Rev. X* **2018**, *8*, 021062. [CrossRef]
20. Bertini, B.; Kos, P.; Prosen, T. Exact Spectral Form Factor in a Minimal Model of Many-Body Quantum Chaos. *Phys. Rev. Lett.* **2018**, *121*, 264101. [CrossRef]
21. Friedman, A.J.; Chan, A.; De Luca, A.; Chalker, J.T. Spectral Statistics and Many-Body Quantum Chaos with Conserved Charge. *Phys. Rev. Lett.* **2019**, *123*, 210603. [CrossRef]
22. Kobrin, B.; Yang, Z.; Kahanamoku-Meyer, G.D.; Olund, C.T.; Moore, J.E.; Stanford, D.; Yao, N.Y. Many-Body Chaos in the Sachdev-Ye-Kitaev Model. *Phys. Rev. Lett.* **2021**, *126*, 030602. [CrossRef]
23. Bertini, B.; Kos, P.; Prosen, T. Entanglement Spreading in a Minimal Model of Maximal Many-Body Quantum Chaos. *Phys. Rev. X* **2019**, *9*, 021033. [CrossRef]
24. Cvitanovic, P.; Artuso, R.; Mainieri, R.; Tanner, G.; Vattay, G.; Whelan, N.; Wirzba, A. *Chaos: Classical and Quantum*; ChaosBook. org; Niels Bohr Institute: Copenhagen, Denmark, 2005; Volume 69, p. 25.
25. Lichtenberg, A.J.; Lieberman, M.A. *Regular and Chaotic Dynamics*; Springer Science & Business Media: Berlin/Heidelberg, Germany, 2013; Volume 38.
26. Arnol'd, V.I. *Mathematical Methods of Classical Mechanics*; Springer Science & Business Media: Berlin/Heidelberg, Germany, 2013; Volume 60.
27. Berry, M.V.; Tabor, M. Level clustering in the regular spectrum. *Proc. R. Soc. A* **1977**, *356*, 375–394. [CrossRef]
28. Bohigas, O.; Giannoni, M.J.; Schmit, C. Characterization of Chaotic Quantum Spectra and Universality of Level Fluctuation Laws. *Phys. Rev. Lett.* **1984**, *52*, 1–4. [CrossRef]
29. Stöckmann, H.J. *Quantum Chaos: An Introduction*; American Association of Physics Teachers: College Park, MD, USA, 2000.
30. Brody, T.A.; Flores, J.; French, J.B.; Mello, P.A.; Pandey, A.; Wong, S.S.M. Random-matrix physics: Spectrum and strength fluctuations. *Rev. Mod. Phys.* **1981**, *53*, 385–479. [CrossRef]
31. Haake, F. *Quantum Signatures of Chaos*; Springer: Berlin/Heidelberg, Germany, 2010.
32. Izrailev, F.M. Simple models of quantum chaos: Spectrum and eigenfunctions. *Phys. Rep.* **1990**, *196*, 299–392. [CrossRef]
33. Oganesyan, V.; Huse, D.A. Localization of interacting fermions at high temperature. *Phys. Rev. B* **2007**, *75*, 155111. [CrossRef]
34. Atas, Y.Y.; Bogomolny, E.; Giraud, O.; Roux, G. Distribution of the Ratio of Consecutive Level Spacings in Random Matrix Ensembles. *Phys. Rev. Lett.* **2013**, *110*, 084101. [CrossRef] [PubMed]
35. Mehta, M.L. *Random Matrices*; Elsevier: Amsterdam, The Netherlands, 2004.
36. Berry, M.V. Regular and irregular semiclassical wavefunctions. *J. Phys. A* **1977**, *10*, 2083–2091. [CrossRef]
37. Porter, C.E.; Thomas, R.G. Fluctuations of Nuclear Reaction Widths. *Phys. Rev.* **1956**, *104*, 483–491. [CrossRef]
38. Kus, M.; Mostowski, J.; Haake, F. Universality of eigenvector statistics of kicked tops of different symmetries. *J. Phys. A* **1988**, *21*, L1073–L1077. [CrossRef]
39. Alhassid, Y.; Levine, R.D. Transition-Strength Fluctuations and the Onset of Chaotic Motion. *Phys. Rev. Lett.* **1986**, *57*, 2879–2882. [CrossRef]
40. Alhassid, Y.; Feingold, M. Statistical fluctuations of matrix elements in regular and chaotic systems. *Phys. Rev. A* **1989**, *39*, 374–377. [CrossRef] [PubMed]
41. Haake, F.; Życzkowski, K. Random-matrix theory and eigenmodes of dynamical systems. *Phys. Rev. A* **1990**, *42*, 1013–1016. [CrossRef] [PubMed]
42. Zyczkowski, K. Indicators of quantum chaos based on eigenvector statistics. *J. Phys. A* **1990**, *23*, 4427. [CrossRef]
43. Leboeuf, P.; Voros, A. Chaos-revealing multiplicative representation of quantum eigenstates. *J. Phys. A* **1990**, *23*, 1765–1774. [CrossRef]
44. Batistić, B.; Robnik, M. Quantum localization of chaotic eigenstates and the level spacing distribution. *Phys. Rev. E* **2013**, *88*, 052913. [CrossRef] [PubMed]
45. Bastarrachea-Magnani, M.A.; López-del Carpio, B.; Chávez-Carlos, J.; Lerma-Hernández, S.; Hirsch, J.G. Delocalization and quantum chaos in atom-field systems. *Phys. Rev. E* **2016**, *93*, 022215. [CrossRef] [PubMed]
46. Bastarrachea-Magnani, M.A.; del Carpio, B.L.; Chávez-Carlos, J.; Lerma-Hernández, S.; Hirsch, J.G. Regularity and chaos in cavity QED. *Phys. Scr.* **2017**, *92*, 054003. [CrossRef]

47. Mondal, D.; Sinha, S.; Sinha, S. Chaos and quantum scars in a coupled top model. *Phys. Rev. E* **2020**, *102*, 020101. [CrossRef] [PubMed]

48. Wang, Q.; Robnik, M. Statistical properties of the localization measure of chaotic eigenstates in the Dicke model. *Phys. Rev. E* **2020**, *102*, 032212. [CrossRef] [PubMed]

49. Villaseñor, D.; Pilatowsky-Cameo, S.; Bastarrachea-Magnani, M.A.; Lerma-Hernández, S.; Hirsch, J.G. Quantum localization measures in phase space. *Phys. Rev. E* **2021**, *103*, 052214. [CrossRef] [PubMed]

50. Sreenivasan, K.R. Fractals and Multifractals in Fluid Turbulence. *Annu. Rev. Fluid Mech.* **1991**, *23*, 539–604. [CrossRef]

51. Stanley, H.E.; Meakin, P. Multifractal phenomena in physics and chemistry. *Nature* **1988**, *335*, 405–409. [CrossRef]

52. Jiang, Z.Q.; Xie, W.J.; Zhou, W.X.; Sornette, D. Multifractal analysis of financial markets: A review. *Rep. Prog. Phys.* **2019**, *82*, 125901. [CrossRef]

53. Mirlin, A.D.; Evers, F. Multifractality and critical fluctuations at the Anderson transition. *Phys. Rev. B* **2000**, *62*, 7920–7933. [CrossRef]

54. Tarzia, M. Many-body localization transition in Hilbert space. *Phys. Rev. B* **2020**, *102*, 014208. [CrossRef]

55. Evers, F.; Mirlin, A.D. Anderson transitions. *Rev. Mod. Phys.* **2008**, *80*, 1355–1417. [CrossRef]

56. Rodriguez, A.; Vasquez, L.J.; Slevin, K.; Römer, R.A. Multifractal finite-size scaling and universality at the Anderson transition. *Phys. Rev. B* **2011**, *84*, 134209. [CrossRef]

57. Macé, N.; Alet, F.; Laflorencie, N. Multifractal Scalings Across the Many-Body Localization Transition. *Phys. Rev. Lett.* **2019**, *123*, 180601. [CrossRef]

58. Solórzano, A.; Santos, L.F.; Torres-Herrera, E.J. Multifractality and self-averaging at the many-body localization transition. *arXiv* **2021**, arXiv:2102.02824.

59. Atas, Y.Y.; Bogomolny, E. Multifractality of eigenfunctions in spin chains. *Phys. Rev. E* **2012**, *86*, 021104. [CrossRef]

60. Luitz, D.J.; Alet, F.; Laflorencie, N. Universal Behavior beyond Multifractality in Quantum Many-Body Systems. *Phys. Rev. Lett.* **2014**, *112*, 057203. [CrossRef] [PubMed]

61. Lindinger, J.; Buchleitner, A.; Rodríguez, A. Many-Body Multifractality throughout Bosonic Superfluid and Mott Insulator Phases. *Phys. Rev. Lett.* **2019**, *122*, 106603. [CrossRef] [PubMed]

62. Atas, Y.Y.; Bogomolny, E. Calculation of multi-fractal dimensions in spin chains. *Philos. Trans. R. Soc. A* **2014**, *372*, 20120520. [CrossRef]

63. Martin, J.; García-Mata, I.; Giraud, O.; Georgeot, B. Multifractal wave functions of simple quantum maps. *Phys. Rev. E* **2010**, *82*, 046206. [CrossRef]

64. Bogomolny, E.; Giraud, O. Eigenfunction Entropy and Spectral Compressibility for Critical Random Matrix Ensembles. *Phys. Rev. Lett.* **2011**, *106*, 044101. [CrossRef]

65. García-Mata, I.; Martin, J.; Giraud, O.; Georgeot, B. Multifractality of quantum wave packets. *Phys. Rev. E* **2012**, *86*, 056215. [CrossRef] [PubMed]

66. De Tomasi, G.; Khaymovich, I.M. Multifractality Meets Entanglement: Relation for Nonergodic Extended States. *Phys. Rev. Lett.* **2020**, *124*, 200602. [CrossRef] [PubMed]

67. Bilen, A.M.; Georgeot, B.; Giraud, O.; Lemarié, G.; García-Mata, I. Symmetry violation of quantum multifractality: Gaussian fluctuations versus algebraic localization. *Phys. Rev. Res.* **2021**, *3*, L022023. [CrossRef]

68. Bäcker, A.; Haque, M.; Khaymovich, I.M. Multifractal dimensions for random matrices, chaotic quantum maps, and many-body systems. *Phys. Rev. E* **2019**, *100*, 032117. [CrossRef]

69. Pausch, L.; Carnio, E.G.; Rodríguez, A.; Buchleitner, A. Chaos and Ergodicity across the Energy Spectrum of Interacting Bosons. *Phys. Rev. Lett.* **2021**, *126*, 150601. [CrossRef] [PubMed]

70. Bilen, A.M.; García-Mata, I.; Georgeot, B.; Giraud, O. Multifractality of open quantum systems. *Phys. Rev. E* **2019**, *100*, 032223. [CrossRef]

71. Haake, F.; Kuś, M.; Scharf, R. Classical and quantum chaos for a kicked top. *Z. Phys. B* **1987**, *65*, 381–395. [CrossRef]

72. Fox, R.F.; Elston, T.C. Chaos and a quantum-classical correspondence in the kicked top. *Phys. Rev. E* **1994**, *50*, 2553–2563. [CrossRef]

73. Trail, C.M.; Madhok, V.; Deutsch, I.H. Entanglement and the generation of random states in the quantum chaotic dynamics of kicked coupled tops. *Phys. Rev. E* **2008**, *78*, 046211. [CrossRef]

74. Lombardi, M.; Matzkin, A. Entanglement and chaos in the kicked top. *Phys. Rev. E* **2011**, *83*, 016207. [CrossRef]

75. Sieberer, L.M.; Olsacher, T.; Elben, A.; Heyl, M.; Hauke, P.; Haake, F.; Zoller, P. Digital quantum simulation, Trotter errors, and quantum chaos of the kicked top. *NPJ Quantum Inf.* **2019**, *5*, 78. [CrossRef]

76. Dogra, S.; Madhok, V.; Lakshminarayan, A. Quantum signatures of chaos, thermalization, and tunneling in the exactly solvable few-body kicked top. *Phys. Rev. E* **2019**, *99*, 062217. [CrossRef] [PubMed]

77. Muñoz Arias, M.H.; Poggi, P.M.; Jessen, P.S.; Deutsch, I.H. Simulating Nonlinear Dynamics of Collective Spins via Quantum Measurement and Feedback. *Phys. Rev. Lett.* **2020**, *124*, 110503. [CrossRef]

78. Muñoz Arias, M.H.; Poggi, P.M.; Deutsch, I.H. Nonlinear dynamics and quantum chaos of a family of kicked *p*-spin models. *Phys. Rev. E* **2021**, *103*, 052212. [CrossRef]

79. Chaudhury, S.; Smith, A.; Anderson, B.E.; Ghose, S.; Jessen, P.S. Quantum signatures of chaos in a kicked top. *Nature* **2009**, *461*, 768–771. [CrossRef]

80. Neill, C.; Roushan, P.; Fang, M.; Chen, Y.; Kolodrubetz, M.; Chen, Z.; Megrant, A.; Barends, R.; Campbell, B.; Chiaro, B.; et al. Ergodic dynamics and thermalization in an isolated quantum system. *Nat. Phys.* **2016**, *12*, 1037–1041. [CrossRef]

81. Tomkovič, J.; Muessel, W.; Strobel, H.; Löck, S.; Schlagheck, P.; Ketzmerick, R.; Oberthaler, M.K. Experimental observation of the Poincaré-Birkhoff scenario in a driven many-body quantum system. *Phys. Rev. A* **2017**, *95*, 011602. [CrossRef]

82. Meier, E.J.; Ang'ong'a, J.; An, F.A.; Gadway, B. Exploring quantum signatures of chaos on a Floquet synthetic lattice. *Phys. Rev. A* **2019**, *100*, 013623. [CrossRef]

83. Wang, X.; Ma, J.; Song, L.; Zhang, X.; Wang, X. Spin squeezing, negative correlations, and concurrence in the quantum kicked top model. *Phys. Rev. E* **2010**, *82*, 056205. [CrossRef] [PubMed]

84. Caiani, L.; Casetti, L.; Clementi, C.; Pettini, M. Geometry of Dynamics, Lyapunov Exponents, and Phase Transitions. *Phys. Rev. Lett.* **1997**, *79*, 4361–4364. [CrossRef]

85. Vallejos, R.O.; Anteneodo, C. Theoretical estimates for the largest Lyapunov exponent of many-particle systems. *Phys. Rev. E* **2002**, *66*, 021110. [CrossRef] [PubMed]

86. Parker, T.S.; Chua, L. *Practical Numerical Algorithms for Chaotic Systems*; Springer Science & Business Media: Berlin/Heidelberg, Germany, 2012.

87. Oseledets, V.I. A multiplicative ergodic theorem. Characteristic Lyapunov, exponents of dynamical systems. *Trans. Moscow Math. Soc.* **1968**, *19*, 179–210.

88. Constantoudis, V.; Theodorakopoulos, N. Lyapunov exponent, stretching numbers, and islands of stability of the kicked top. *Phys. Rev. E* **1997**, *56*, 5189–5194. [CrossRef]

89. Bhosale, U.T.; Santhanam, M.S. Periodicity of quantum correlations in the quantum kicked top. *Phys. Rev. E* **2018**, *98*, 052228. [CrossRef]

90. D'Ariano, G.M.; Evangelista, L.R.; Saraceno, M. Classical and quantum structures in the kicked-top model. *Phys. Rev. A* **1992**, *45*, 3646–3658. [CrossRef] [PubMed]

91. Kolmogorov, A.N. A New Metric Invariant of Transient Dynamical Systems and Automorphisms in Lebesgue Spaces. *Dokl. Akad. Nauk SSSR* **1958**, *119*, 861–864.

92. Kolmogorov, A.N. Entropy per Unit Time as a Metric Invariant of Automorphisms. *Dokl. Akad. Nauk SSSR* **1959**, *124*, 754–755.

93. Pesin, Y.B. Characteristic Lyapunov exponents and smooth ergodic theory. *Russ. Mat. Surv.* **1977**, *32*, 55–112. [CrossRef]

94. Furuya, K.; Nemes, M.C.; Pellegrino, G.Q. Quantum Dynamical Manifestation of Chaotic Behavior in the Process of Entanglement. *Phys. Rev. Lett.* **1998**, *80*, 5524–5527. [CrossRef]

95. Lakshminarayan, A. Entangling power of quantized chaotic systems. *Phys. Rev. E* **2001**, *64*, 036207. [CrossRef]

96. Seshadri, A.; Madhok, V.; Lakshminarayan, A. Tripartite mutual information, entanglement, and scrambling in permutation symmetric systems with an application to quantum chaos. *Phys. Rev. E* **2018**, *98*, 052205. [CrossRef]

97. Gietka, K.; Chwedeńczuk, J.; Wasak, T.; Piazza, F. Multipartite entanglement dynamics in a regular-to-ergodic transition: Quantum Fisher information approach. *Phys. Rev. B* **2019**, *99*, 064303. [CrossRef]

98. Emerson, J.; Weinstein, Y.S.; Lloyd, S.; Cory, D.G. Fidelity Decay as an Efficient Indicator of Quantum Chaos. *Phys. Rev. Lett.* **2002**, *89*, 284102. [CrossRef]

99. Torres-Herrera, E.J.; Santos, L.F. Dynamical manifestations of quantum chaos: Correlation hole and bulge. *Philos. Trans. R. Soc. A* **2017**, *375*, 20160434. [CrossRef] [PubMed]

100. Rozenbaum, E.B.; Ganeshan, S.; Galitski, V. Lyapunov Exponent and Out-of-Time-Ordered Correlator's Growth Rate in a Chaotic System. *Phys. Rev. Lett.* **2017**, *118*, 086801. [CrossRef]

101. García-Mata, I.; Saraceno, M.; Jalabert, R.A.; Roncaglia, A.J.; Wisniacki, D.A. Chaos Signatures in the Short and Long Time Behavior of the Out-of-Time Ordered Correlator. *Phys. Rev. Lett.* **2018**, *121*, 210601. [CrossRef]

102. Chávez-Carlos, J.; López-del Carpio, B.; Bastarrachea-Magnani, M.A.; Stránský, P.; Lerma-Hernández, S.; Santos, L.F.; Hirsch, J.G. Quantum and Classical Lyapunov Exponents in Atom-Field Interaction Systems. *Phys. Rev. Lett.* **2019**, *122*, 024101. [CrossRef]

103. Fortes, E.M.; García-Mata, I.; Jalabert, R.A.; Wisniacki, D.A. Gauging classical and quantum integrability through out-of-time-ordered correlators. *Phys. Rev. E* **2019**, *100*, 042201. [CrossRef] [PubMed]

104. Wigner, E.P. On the Distribution of the Roots of Certain Symmetric Matrices. *Ann. Math.* **1958**, *67*, 325–327. [CrossRef]

105. Heusler, S.; Müller, S.; Altland, A.; Braun, P.; Haake, F. Periodic-Orbit Theory of Level Correlations. *Phys. Rev. Lett.* **2007**, *98*, 044103. [CrossRef] [PubMed]

106. Nagao, T.; Müller, S. Then-level spectral correlations for chaotic systems. *J. Phys. A* **2009**, *42*, 375102. [CrossRef]

107. Müller, S.; Novaes, M. Semiclassical calculation of spectral correlation functions of chaotic systems. *Phys. Rev. E* **2018**, *98*, 052207. [CrossRef]

108. Müller, S.; Novaes, M. Full perturbative calculation of spectral correlation functions for chaotic systems in the unitary symmetry class. *Phys. Rev. E* **2018**, *98*, 052208. [CrossRef]

109. Zeldovich, Y.B. The quasienergy of quantum-mechanical system subjected to a periodic action. *Z. Eksper. Teor. Fiz.* **1966**, *51*, 1492.

110. Prosen, T.; Robnik, M. Semiclassical energy level statistics in the transition region between integrability and chaos: Transition from Brody-like to Berry-Robnik behaviour. *J. Phys. A* **1994**, *27*, 8059–8077. [CrossRef]

111. Berry, M.V.; Robnik, M. Semiclassical level spacings when regular and chaotic orbits coexist. *J. Phys. A* **1984**, *17*, 2413–2421. [CrossRef]

112. Klauder, J.R.; Skagerstam, B.S. *Coherent States: Applications in Physics and Mathematical Physics*; World Scientific: Singapore, 1985.

113. Zhang, W.M.; Feng, D.H.; Gilmore, R. Coherent states: Theory and some applications. *Rev. Mod. Phys.* **1990**, *62*, 867–927. [CrossRef]
114. Gazeau, J.P. *Coherent States in Quantum Optics*; Wiley-VCH: Berlin, Germany, 2009.
115. Robert, D.; Combescure, M. *Coherent States and Applications in Mathematical Physics*; Springer: Berlin/Heidelberg, Germany, 2012.
116. Antoine, J.P.; Bagarello, F.; Gazeau, J.P. *Coherent States and Their Applications*; Springer: Berlin/Heidelberg, Germany, 2018.
117. Radcliffe, J.M. Some properties of coherent spin states. *J. Phys. A* **1971**, *4*, 313–323. [CrossRef]
118. Kuś, M.; Zakrzewski, J.; Życzkowski, K. Quantum scars on a sphere. *Phys. Rev. A* **1991**, *43*, 4244–4248. [CrossRef]
119. Stéphan, J.M.; Misguich, G.; Pasquier, V. Phase transition in the Rényi-Shannon entropy of Luttinger liquids. *Phys. Rev. B* **2011**, *84*, 195128. [CrossRef]
120. Visscher, W. Localization of electron wave functions in disordered systems. *J. Non-Cryst. Solids* **1972**, *8–10*, 477–484. [CrossRef]
121. Fyodorov, Y.V.; Giraud, O. High values of disorder-generated multifractals and logarithmically correlated processes. *Chaos Solitons Fractals* **2015**, *74*, 15–26. Extreme Events and its Applications. [CrossRef]
122. Brickmann, J.; Engel, Y.; Levine, R. The distribution of intensities in a vibrational spectrum: A model computational study of the transition to classical chaos. *Chem. Phys. Lett.* **1987**, *137*, 441–447. [CrossRef]
123. Kullback, S.; Leibler, R.A. On Information and Sufficiency. *Ann. Math. Stat.* **1951**, *22*, 79–86. [CrossRef]
124. Beugeling, W.; Bäcker, A.; Moessner, R.; Haque, M. Statistical properties of eigenstate amplitudes in complex quantum systems. *Phys. Rev. E* **2018**, *98*, 022204. [CrossRef] [PubMed]
125. Schervish, M.J.; DeGroot, M. *Probability and Statistics*; Pearson Education: London, UK, 2014.
126. Wang, Q.; Pérez-Bernal, F. Characterizing the Lipkin-Meshkov-Glick model excited-state quantum phase transition using dynamical and statistical properties of the diagonal entropy. *Phys. Rev. E* **2021**, *103*, 032109. [CrossRef] [PubMed]
127. Flack, A.; Bertini, B.; Prosen, T. Statistics of the spectral form factor in the self-dual kicked Ising model. *Phys. Rev. Res.* **2020**, *2*, 043403. [CrossRef]
128. Braun, P.; Waltner, D.; Akila, M.; Gutkin, B.; Guhr, T. Transition from quantum chaos to localization in spin chains. *Phys. Rev. E* **2020**, *101*, 052201. [CrossRef]
129. Khramtsov, M.; Lanina, E. Spectral form factor in the double-scaled SYK model. *J. High Energy Phys.* **2021**, *2021*, 31. [CrossRef]
130. Lewis-Swan, R.J.; Safavi-Naini, A.; Bollinger, J.J.; Rey, A.M. Unifying scrambling, thermalization and entanglement through measurement of fidelity out-of-time-order correlators in the Dicke model. *Nat. Commun.* **2019**, *10*, 1581. [CrossRef]
131. Rozenbaum, E.B.; Ganeshan, S.; Galitski, V. Universal level statistics of the out-of-time-ordered operator. *Phys. Rev. B* **2019**, *100*, 035112. [CrossRef]
132. Lee, J.; Kim, D.; Kim, D.H. Typical growth behavior of the out-of-time-ordered commutator in many-body localized systems. *Phys. Rev. B* **2019**, *99*, 184202. [CrossRef]
133. Bergamasco, P.D.; Carlo, G.G.; Rivas, A.M.F. Out-of-time ordered correlators, complexity, and entropy in bipartite systems. *Phys. Rev. Res.* **2019**, *1*, 033044. [CrossRef]
134. Harrow, A.W.; Kong, L.; Liu, Z.W.; Mehraban, S.; Shor, P.W. Separation of Out-Of-Time-Ordered Correlation and Entanglement. *PRX Quantum* **2021**, *2*, 020339. [CrossRef]
135. Leviandier, L.; Lombardi, M.; Jost, R.; Pique, J.P. Fourier Transform: A Tool to Measure Statistical Level Properties in Very Complex Spectra. *Phys. Rev. Lett.* **1986**, *56*, 2449–2452. [CrossRef]
136. Chalker, J.T.; Kravtsov, V.E.; Lerner, I.V. Spectral rigidity and eigenfunction correlations at the Anderson transition. *J. Exp. Theor. Phys. Lett.* **1996**, *64*, 386–392. [CrossRef]
137. Rammensee, J.; Urbina, J.D.; Richter, K. Many-Body Quantum Interference and the Saturation of Out-of-Time-Order Correlators. *Phys. Rev. Lett.* **2018**, *121*, 124101. [CrossRef]
138. Prakash, R.; Lakshminarayan, A. Scrambling in strongly chaotic weakly coupled bipartite systems: Universality beyond the Ehrenfest timescale. *Phys. Rev. B* **2020**, *101*, 121108. [CrossRef]
139. Hosur, P.; Qi, X.L.; Roberts, D.A.; Yoshida, B. Chaos in quantum channels. *J. High Energy Phys.* **2016**, *2016*, 4. [CrossRef]
140. Fan, R.; Zhang, P.; Shen, H.; Zhai, H. Out-of-time-order correlation for many-body localization. *Sci. Bull.* **2017**, *62*, 707–711. [CrossRef]
141. Faez, S.; Strybulevych, A.; Page, J.H.; Lagendijk, A.; van Tiggelen, B.A. Observation of Multifractality in Anderson Localization of Ultrasound. *Phys. Rev. Lett.* **2009**, *103*, 155703. [CrossRef]
142. Lemarié, G.; Lignier, H.; Delande, D.; Szriftgiser, P.; Garreau, J.C. Critical State of the Anderson Transition: Between a Metal and an Insulator. *Phys. Rev. Lett.* **2010**, *105*, 090601. [CrossRef] [PubMed]
143. Richardella, A.; Roushan, P.; Mack, S.; Zhou, B.; Huse, D.A.; Awschalom, D.D.; Yazdani, A. Visualizing Critical Correlations Near the Metal-Insulator Transition in Ga1-xMnxAs. *Science* **2010**, *327*, 665–669. [CrossRef] [PubMed]
144. Sagi, Y.; Brook, M.; Almog, I.; Davidson, N. Observation of Anomalous Diffusion and Fractional Self-Similarity in One Dimension. *Phys. Rev. Lett.* **2012**, *108*, 093002. [CrossRef] [PubMed]